

WAVELENGTH MEASUREMENTS OF K TRANSITIONS OF OXYGEN, NEON, AND MAGNESIUM WITH X-RAY ABSORPTION LINES

Jin-Yuan Liao¹, Shuang-Nan Zhang^{1,2}, Yangsen Yao^{3,4}

ABSTRACT

Accurate atomic transition data are important in many astronomical research areas especially in line spectroscopy study. Whereas transition data of He-like and H-like ions (i.e., ions at high-charge states) are accurately calculated, that of K transitions of neutral or low-ionized metal elements are still very uncertain. Spectroscopy of absorption lines produced in the interstellar medium (ISM) has been proven to be an effective way to measure the central wavelengths of these atomic transitions. In this work we analyze 36 *Chandra High Energy Transmission Grating* observations and search for and measure the ISM absorption lines along sight lines of 11 low-mass X-ray binaries. We correct the Galactic rotation velocity to the rest frame for every observation and then use two different methods to merge all the corrected spectra to a co-added spectrum. However the co-added spectra obtained by these methods exhibit biases, either to the observations of high counts or high signal-to-noise ratios of the lines. We make Bayesian analysis to several significantly detected lines to obtain the systematic uncertainty and the bias correction of other lines. Compared to previous studies (e.g., Yao et al. 2009), our results improve the accuracy of wavelengths by a factor from two to five and significantly reduce the systematic uncertainties and biases. Several weak transitions (e.g., 1s–2p of Mg iv and Mg v; 1s–3p of Mg iii and Mg v) are also detected for the first time, albeit with low significance; future observations with improved accuracy are required to confirm these detections.

Subject headings: X-rays: binaries—X-rays: ISM—ISM: atoms—methods: data analysis

¹Key Laboratory of Particle Astrophysics, Institute of High Energy Physics, Chinese Academy of Sciences, Beijing 100049, China; zhangsn@ihep.ac.cn

²National Astronomical Observatories, Chinese Academy of Sciences, Beijing, 100012, China

³Eureka Scientific, 2452 Delmer Street Suite 100, Oakland, CA 94602

⁴Center for Astrophysics and Space Astronomy, University of Colorado, Boulder, CO 80309, USA

1. INTRODUCTION

Since the launch of modern X-ray space telescopes like *Chandra* and *XMM-Newton* X-ray Observatories, X-ray astronomy has entered the epoch of grating observations that can produce spectra with much improved energy resolution. In these spectra narrow absorption/emission lines, which have never been observed before, now have been commonly detected. These X-ray absorption/emission lines can be generated in a variety of astronomical environments, e.g., stellar coronae (SC), supernova remnants, X-ray binaries (XRBs), galaxies, AGN, and interstellar media (ISM) and intergalactic media (IGM) (e.g., Raassen et al. 2003; Dewey et al. 2008; Schulz et al. 2002; Miller et al. 2006; Steenbrugge et al. 2003; Lee et al. 2001; Yao & Wang 2005; Fang et al. 2003; Nicastro et al. 2005). These lines carry valuable information about the absorbing/emitting material and thus are powerful diagnostic tools for stellar evolution, explosion mechanism of SNe, mass exchange in accretion systems, interplays of different galactic components, feedback of AGN, galaxy formation and evolution, evolution of our universe, and so on. Clearly, proper identifications of these lines and subsequent scientific derivation and interpretation strongly rely on the accuracy of atomic databases of responsible transitions.

There are several available databases of atomic transitions, among which the most commonly referenced four in X-ray community are Verner et al. (1996, hereafter V96), NIST, XSTAR (Kallman et al. 2004), and APED (Smith et al. 2001). While atomic data for ions at high-charge states (e.g., He- and H-like ions) are very accurate in these databases and consistent with observations (Juett et al. 2004, 2006, J0406 hereafter; Yao et al. 2009, Y09 hereafter), those for K transitions of neutral and mildly ionized metal elements (e.g., O I–O III, Ne I–Ne III, Mg III–Mg V, etc.) have not been included in any of them. There also exists other serious problems. First, although the statistical errors of the wavelengths of these high-ionized lines can be less than 10 mÅ in astronomical observations, they are still not enough for the study of the low-velocity gases. Y09 have measured these high-ionized lines; however, some lines have large uncertainties, such as O VIII K β that has a statistical error 6.7 mÅ, equivalent to 125 km s⁻¹. In addition, some lines (e.g., Ne X K α) are too weak to be given statistical errors. Second, the methods commonly used (e.g., Y09) to obtain the co-added spectrum introduce biases, which must be corrected and otherwise will result in serious estimation errors of the gas velocities as well as other parameters associated with the gas velocities. Finally, some of the line wavelengths are not consistent with each other between the commonly referenced databases. For example, the wavelength of O VII K β in NIST is 18.6270 Å but is 18.6288 Å in V96. The difference between the two values is ~ 30 km s⁻¹, which is a serious problem for the study of the low-velocity gas. Therefore, it is essential to make observational identifications of the K-shell transitions of the neutral, low-ionized, and high-ionized metals. Since most of K transitions of these low-ionization ions are in the wavelength range of 9.5–24.0 Å, within which copious lines of highly ionized metal elements have also been observed, these miss-

ing atomic data are important not only for their own rights but also for proper identifications of other lines. Recently, several groups have calculated and updated these databases (e.g., Gorczyca 2000; Behar & Netzer 2002; Gorczyca & McLaughlin 2005; García et al. 2005), but even the centroid wavelengths, the most basic parameters of these lines, are yet to be coincided (see Table 1). In addition, the laboratory measurements are also very uncertain; e.g., the wavelength of O I 1s–2p given by Stolte et al. (1997) range from 23.489 to 23.536 Å.

Some Galactic X-ray sources are very bright in the soft X-ray band. When the X-ray continuous radiations pass through the ISM in different phases, X-ray absorption lines of ions at various charge states are produced and thus are excellent calibration references for these atomic data. For instance, Schattenburg & Canizares (1986) used the Einstein observations of the Crab to obtain the wavelength of the neutral O (1s–2p of O I), although the result is uncertain (23.46 ± 0.22 Å) according to modern standard. J0406 analyzed *Chandra* High Energy Transmission Grating (HETG) observations of several Galactic XRBs and obtained the wavelengths of some strong lines (i.e., 1s–2p of O I, O II, O III, Ne II, Ne III and 1s–3p of O I). They found theoretically calculated line centroids of K transitions of low ionized neon and oxygen need to be shifted > 20 mÅ to match observed values, which corresponds to $300 - 400$ km s⁻¹ shift for oxygen- and neon-absorbers. However, the ISM is rotating around the Galactic center and thus the observed X-ray lines are not at the rest-frame wavelengths. Unfortunately, the above three previous works did not do the Galactic rotation correction. It is also necessary to exclude X-ray sources with significant intrinsic absorptions, such as accreting X-ray binaries with winds from either their companions or accretion disks along the line of sight (LOS). This can be done easily by comparing absorption line and/or total absorption properties of a target with multiple observations, since all X-ray binaries exhibit significant variability.

Although X-ray absorption lines produced in the ISM are indeed ideal sources for calibrating theoretical predictions of atomic transitions, high spectral quality is crucial to accomplishing this important task. The measurements by J0406 are based on relatively poor quality spectra (with signal-to-noise ratio SNR $\lesssim 15$ per 10-mÅ spectral bin) obtained with short observations of several sources; thus only those strong transitions (e.g., 1s–2p of O I, Ne II, and Ne III) were relatively well constrained, and others were still of large uncertainties ($\Delta\lambda \sim 6 - 20$ mÅ) or not observed. Recently Y09 presented an extensive study of ISM X-ray absorption lines in the spectrum of Cyg X–2 observed with the *Chandra*-HETG spectrograph. The high spectral quality not only allowed them to measure most of the transitions listed by J0406 as accurate as $\Delta\lambda \sim 1 - 4$ mÅ (1σ uncertainty) but also enabled them to constrain other faint transitions not included and/or misidentified in their list. For instance, Y09 detected and measured the 1s–3p transition of Ne III that could not be revealed in previous poor quality spectra, and they did not confirm the reported line at 23.140 Å that was misidentified as 1s–3p transition of O III.

Table 1. The wavelengths of low-ionized O, Ne, and Mg from previous work

Ion	Transition	Wavelength (Å)			
		G05BN02	G00GM05	J0406	Y09
O I	1s–2p	23.4475	23.532	23.508	23.508
O I	1s–3p	...	22.907	22.884	...
O II	1s–2p	23.3100	22.781	23.330	23.384
O II	1s–3p	...	22.576
O III	1s–2p	23.0800	...	23.140	...
O III	1s–3p
Ne I	1s–3p	...	14.295	14.295	14.294
Ne II	1s–2p	14.6310	14.608	14.608	14.605
Ne II	1s–3p	14.001
Ne III	1s–2p	14.5260	14.508	14.508	14.507
Ne III	1s–3p	13.690
Mg III	1s–3p
Mg IV	1s–2p
Mg IV	1s–3p

References. — G05BN02: García et al.(2005) and Behar & Netzer (2002); G00GM05: Gorczyca (2000) and Gorczyca & McLaughlin (2005); J0406: Juett et al. (2004, 2006); Y09: Yao et al. (2009).

In this work, our aim is to obtain more accurate K transition data of neutral, low- and high-ionized metals, as well as to find some weak absorption lines (e.g., $1s-2p$ of Mg IV–Mg V; $1s-3p$ of Mg III–Mg V). We jointly analyze 36 *Chandra*-HETG observations of 11 Galactic XRBs and give the most accurate wavelengths for K-shell transitions of neutral, low- and high-ionized atoms. In Section 2 we describe our methods of extracting the X-ray spectra and correcting for the Galactic rotation. In Section 3 we present the results of a joint analysis of all the observational data. In Section 4 we estimate systematic uncertainties and make necessary corrections to the detected lines. A discussion and summary are given in Section 5 and 6, respectively.

2. SAMPLE SELECTION, DATA PROCESSING AND GALACTIC ROTATION CORRECTION

2.1. Sample Selection

In order to obtain high SNR continuum spectra and absorption lines, we adopt the following criteria to select the sample:

- Only the Galactic low-mass X-ray binaries (LMXBs) are used as the background light sources. Compared to extragalactic sources (e.g., AGNs), Galactic XRBs are usually located at low Galactic latitudes and thus the column densities of the ISM along the LOS are usually large if they are not too close to us. Thus strong absorption lines are expected in their spectra. High mass X-ray binaries are excluded to avoid any possible contamination caused by their stellar winds that may not be stationary (e.g., Cyg X–1; Schulz et al. 2002);
- Sources with intrinsic absorptions or emissions (e.g., GX 339–4, Miller et al. 2004; 4U 1916–05, Juett & Chakrabarty 2006) are excluded;
- Only sources with Galactic latitudes more than 2 degrees are chosen to avoid too heavy Galactic absorptions. Most lines we concern are at wavelengths above 10 \AA and the photons in this band suffer heavy absorption in the Galactic plane, which can reduce the significance of the line fitting (Appendix A);
- Only HETG observations are used to assure a high spectral resolution;
- In order to ensure that there are significant absorption lines, we only include the sources for which the strongest O line ($1s-2p$ of O I) and the strongest Ne line ($1s-2p$ of Ne II) (Figures 1 and 2) are detected in the pipe-line-produced spectra. We choose Ne II $K\alpha$ as an indicator, although it is always intrinsically weaker than O I $K\alpha$ lines; the latter are not detected from

several sources due to the rapidly decreasing effective area of the HETG at wavelengths longer than 20 Å.

Finally, 36 *Chandra*-HETG observations of 11 LMXBs are selected as listed in Table 2.

2.2. Data Reduction

We analyze all observations using CIAO 4.4 and CALDB 4.4.7. We use the standard tool *tgextract* to extract the spectra, i.e. PHA files. The energy redistribution matrix file (RMF) and the ancillary response file (ARF) are made by the standard tools *mkgrmf* and *fullgarf* respectively. All the steps follow the standard procedures except for the determination of the position of the zeroth-order image of each source, which is the key to fix the wavelength scale. Since all the targets in our sample are bright sources, the zeroth-order source images are expected to be either severely piled-up in observations with the timed exposure (TE) mode or have been compressed onto several pixels in observations with the continuous clocking (CC) mode. Rather than following the standard script to find the source positions, we use the mean position of the crosses between the CCD read-out streaks and each of the two arms (HEG and MEG) as the source positions for TE-mode observations, and use two Gaussian profiles to fit the compressed image to determine the source positions for CC-mode observations.

2.3. Velocity Correction due to the Galactic Rotation

Our purpose is to obtain the wavelengths of the absorption lines accurately and thus we must correct for the fact that the line-absorbing gas is not at rest with respect to the local standard rest frame (LSR). The gas in the Galactic plane is rotating around the Galactic center and the rotation velocity increases as the radius decreases. The absorption lines in X-ray band are produced by the multi-phase ISM along the LOS, and the motions are also different for the ISM in different phases. Therefore, we must correct the Galactic rotation of neutral, low-ionized gas, and high-ionized gas separately. We adopt the method in Y09 that assumes that the gas is rotating around the Galactic center approximately in circular orbit and the closer to the Galactic center the faster gas rotates. For gas in radius R and with a rotational speed V , the velocity relative to the LSR is

$$V_r = V_{r, \text{ gas}} - V_{r, \text{ sun}} = R_0 \cos b \sin l \left(\frac{V}{R} - \frac{V_0}{R_0} \right), \quad (1)$$

where

$$R = \sqrt{R_0^2 + D^2 \cos^2 b + 2DR_0 \cos b \cos l}, \quad (2)$$

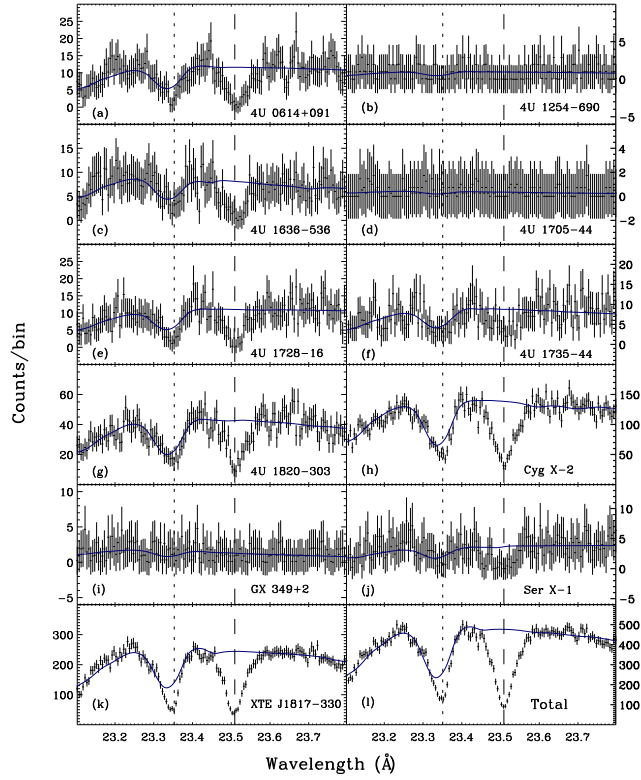


Fig. 1.— Panels (a) to (k) present the positions of the absorption lines of O I $K\alpha$ (dashed line) and O II $K\alpha$ (dotted line) of the targets we selected to study. The co-added spectrum of all the 11 targets is shown in panel (l).

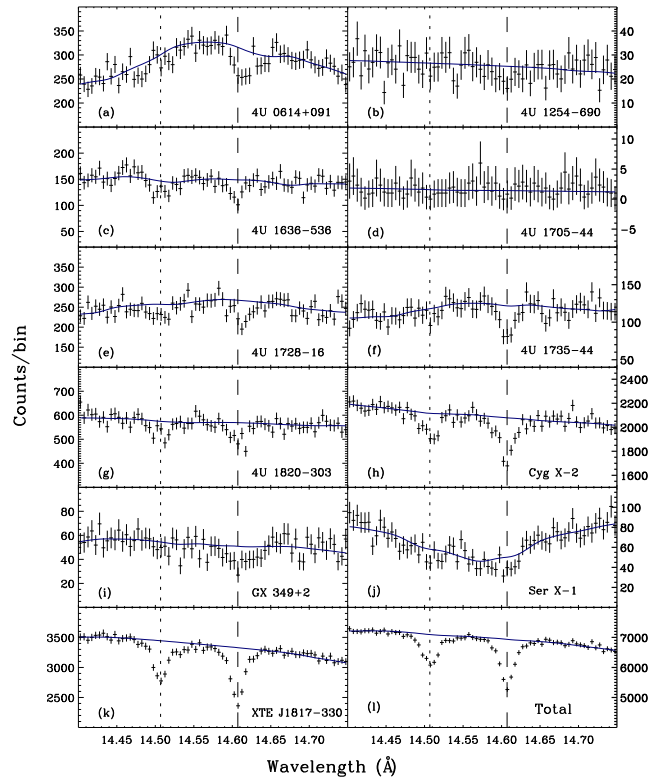


Fig. 2.— The same as Figure 1, but the positions of the absorption lines of Ne II $K\alpha$ (dashed line) and Ne III $K\alpha$ (dotted line) are shown.

Table 2. Targets in our sample

Src.name	(l, b)	Obs.ID	EXPT (ks)	ACR (count s ⁻¹)	Distance (kpc)	V_l (km s ⁻¹)	V_h (km s ⁻¹)
4U 1705–44	(343.32, -2.36)	1923	25	117	5.8 ^a	-17	-37
		1924	6	171
		5500	27	37
GX 349+2	(349.10, 2.75)	715	11	267	5.0 ^c	-7	-10
		3354	35	281
		6628	13	301
		7336	12	264
4U 0614+091	(200.88, -3.36)	10759	60	42	3.2 ^b	19	36
		10760	45	45
		10857	59	62
		10858	35	39
4U 1636–536	(332.92, -4.82)	105	30	105	5.95 ^a	-14	-45
		1939	27	93
		6635	23	41
		6636	25	102
Ser X–1	(36.12, 4.84)	700	78	110	7.7 ^a	14	57
4U 1254–690	(303.48, -6.42)	3823	53	27	15.5 ^a	-2	15
4U 1735–44	(346.05, -6.70)	704	25	92	6.5 ^a	-3	-8
		6637	24	103
		6638	23	110
4U 1820–303	(2.79, -7.91)	1021	10	124	4.94 ^a	6	-1
		1022	11	142
		6633	25	215
		6634	25	272
		7032	46	242
XTE J1817–330	(359.82, -8.00)	6615	50	998	5.0 ^c	7	0
		6616	50	560
		6617	47	293
		6618	51	109
4U 1728–16	(8.51, 9.04)	703	21	129	5.0 ^c	7	-2
		11072	98	118
Cyg X–2	(87.33, -11.32)	1016	15	280	11.0 ^a	-8	-54
		1102	29	130
		8170	77	384
		8599	71	382
		10881	67	267

Note. — We obtained the distances of the targets from: a. Galloway et al. (2008); b. Kuulkers et al. (2010); c. We use the values from Kong (2006), Iaria et al. (2004) and Sala et al. (2007), since the distances of these sources have not been confirmed. ‘EXPT’ in column 4 is the exposure time and ‘ACR’ in column 5 is the average counts rate of every Obs.ID. V_l and V_h in column 7 and 8 are the velocities relative to the LSR of the low-ionized and high-ionized gases respectively.

here D is the distance between the gas and the observer, R_0 and V_0 are the radius of the LSR and its rotation velocity, respectively (Sparke & Gallagher 2000). The average velocity can be obtained by integrating all the gas with different R and V along the path to the source.

For low-ionized gas, we use the neutral H I 21cm emission to trace the gas velocity. Data are derived from the Leiden Argentine Bonn (LAB) Galactic H I Survey (Kalberla et al. 2005) that has a $\sim 30'$ spatial grid and 1.3 km s^{-1} velocity resolution. To obtain the average profile (ϕ_m) of the H I 21cm emission toward the source, we average the emission profiles from the four adjacent H I observations with respect to their angular separations, i.e.,

$$\phi_m = \frac{\sum_{i=1}^4 \phi_i / d_i^2}{\sum_{i=1}^4 1 / d_i^2}, \quad (3)$$

where ϕ_i is the profile of the H I 21cm emission along each individual LOS and d_i is the angular separation between the LOS and the source. Then we can obtain the average H I velocity from ϕ_m and use this value as the projected velocity of the neutral or low-ionized gas along the LOS.

For high-ionized gas, as its scale height is much larger than the low-ionized gas, the halo-lagging effect (Rand 1997, 2000) must be considered. Here, we follow the three assumptions in Y09: (1) the density of the hot gas is $n = n_0 e^{-z/z_n}$, where n_0 is the gas density in the Galactic plane and z is the height from the Galactic plane and $z_n = 3 \text{ kpc}$ (e.g., Bowen et al. 2008; Yao et al. 2008); (2) the rotation velocity linearly decreases from V_0 to zero at a height $z_0 = 8 \text{ kpc}$ (Rand 1997) above the Galactic disk; (3) the velocity at radii between R_0 and R can be linearly interpolated from V_0 and V . For the LSR, we take $R_0 = 8 \text{ kpc}$ and $V_0 = 220 \text{ km s}^{-1}$. The rotation velocity near the target can be inferred from the smallest (largest) velocity of the H I emission and then the average velocity of the hot gas can be obtained by integrating all the gas with different R and V in LOS. The average velocities of the neutral or low-ionized gas and high-ionized hot gas are listed in Table 2.

We transform all the spectra to the LSR and then use the IDL scripts *writepha* and *wrt_ogip_rmf* to produce the spectrum file (PHA) and the response file (RSP = RMF \times ARF) respectively.

3. MERGING SPECTRA AND DETERMINATION OF THE LINE CENTRAL WAVELENGTHS

In this section, we use two different methods to jointly analyze these 36 observations to obtain the wavelengths of the absorption lines of neutral, low-ionized, moderate-ionized and high-ionized gas (Table 4). The result and discussion will be presented in Sections 5 and 6.

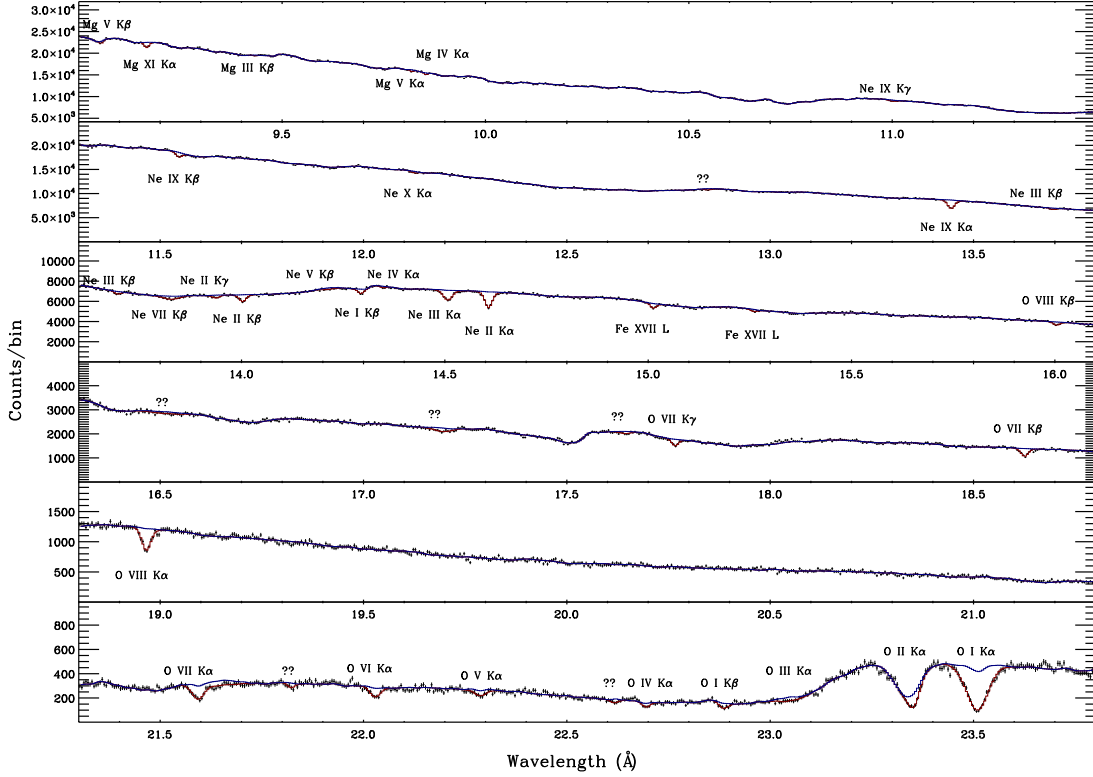


Fig. 3.— Co-added MEG spectrum with the best-fit continuum (thick blue lines). Red histograms mark the observed absorption lines and question marks indicate those unidentified ones.

3.1. Method 1: Direct Merging of All Full Spectra

The entire 36 spectra are co-added by the following two steps to increase the SNR as the method described in Y09: (1) add the counts of each spectrum channel by channel to make a new spectrum file (PHA); (2) merge all the response files to Producing the response file (RSP), where we use the total counts as the weights of each observation.

We fit the co-added spectrum with XSPEC (version 12.7.0) to analyze the co-added spectrum. The continuum is fitted using a power-law plus several broad Gaussian functions and the absorption line is fitted by a narrow Gaussian function,

$$\phi(\lambda_i) = a \frac{1}{\sqrt{2\pi}b} e^{-\frac{(\lambda_i - \lambda)^2}{2b^2}}, \quad (4)$$

where λ is the wavelength of the line centroid, b is the width of the line and a is the normalization of the line. From Figures 3 and 4, it can be seen that the co-added spectrum has very high SNR. As a result, many weak lines (e.g., O VII K γ) are visible. The SNRs around the O I K α , Ne II K α , and Mg XI K α lines are about 20, 80, 110 respectively.

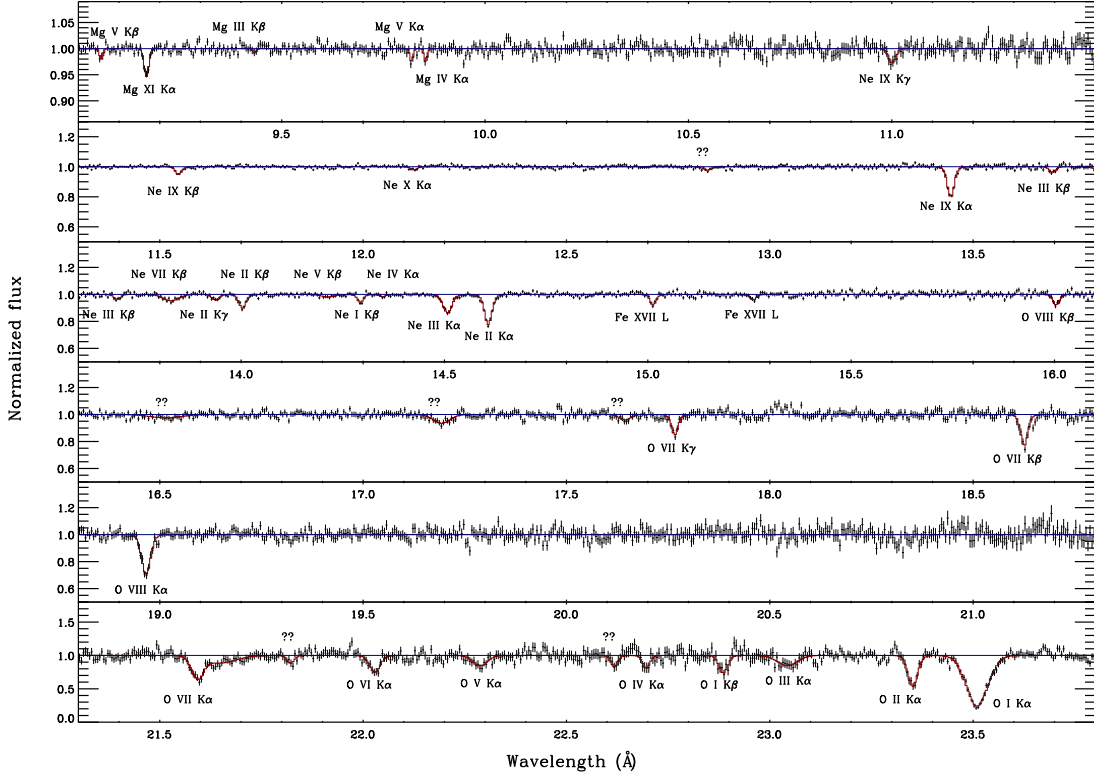


Fig. 4.— The same as Figure 1, but the spectrum is normalized to the best-fit continuum.

Merging the spectra by this method can generally increase the SNR significantly. However, the spectra with weak lines may also weaken the SNR. We take two observations (ObsID 6618 and 8599) as examples. The wavelength of O VI K α is 21.592^{+14}_{-7} Å obtained from the ObsID 6618, whereas it is 21.597^{+15}_{-10} Å from the co-added spectrum with ObsID 6618 and 8599. The error actually increases as more observations are combined, since the significance of the absorption line in ObsID 8599 is too low to increase the significance of the line in the co-added spectrum. As a result, the spectrum with weak absorption lines can only increase the total counts of the continuum, which increases the background noise to the line (Figure 5). To avoid this problem, another method of merging the spectra is investigated next.

3.2. Method 2: Weighted Merging of Net Lines

Unlike the method in Section 3.1, we fit the spectrum to obtain the continuum and line parameters (λ , b , and a) of each observation first. All data for each line flux are then merged to produce

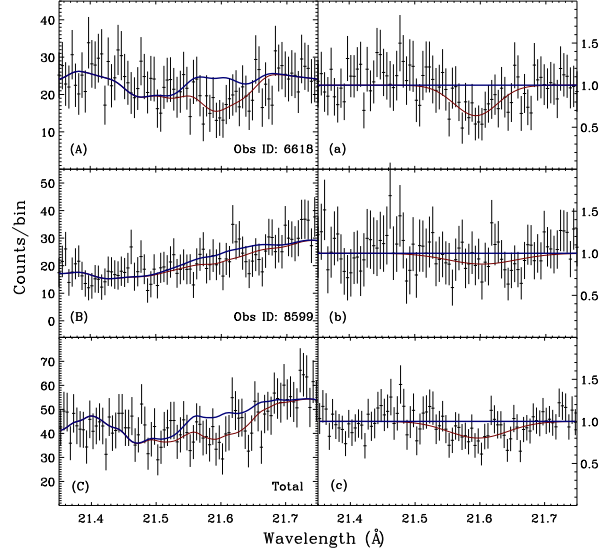


Fig. 5.— The O VII K α line in Obs-ID 6618, 8599, and the co-added spectrum. The right column is normalized to the best-fit continuum.

a co-added line flux after the removal of the continuum of each individual spectrum,

$$f_{\text{add}} = \frac{\sum_{i=1}^{36} f_i w_i}{\sum_{i=1}^{36} w_i}, \quad (5)$$

where f_{add} is the flux of each co-added line flux, f_i and w_i are the flux and weight for each line in each observation. In order to avoid the problem caused by the spectrum with weak ISM absorption, we must evaluate w_i carefully. Here, the weight of each absorption line is given as (Appendix B)

$$w_i = \frac{a_i}{\sigma_i^2 b_i}, \quad (6)$$

where σ_i is the error of the continuum around the line, a_i and b_i are the same as that defined in Equation (4).

For the strong lines (e.g., O I K α and Ne II K α), the significance is high enough to determine the line parameters for most observations, which can be used as the weight to merge the spectra. However, the significance of the weak lines (e.g., O III K α and Ne III K β) is too low and the line parameters can be obtained only in few observations. Among all the 36 observations, $N(\text{Ne II K}\alpha; \text{SNR} > 1.645) = 26$; but $N(\text{Ne III K}\beta; \text{SNR} > 1.645) = 3$. To solve this problem, we make a simple assumption that the clouds in every LOS have the same ion fraction (i.e., all the lines in each spectrum have the same line-strength ratios). The ratios O I K α /O II K α , O VIII K α /O VII K β , and Ne II K α /Ne III K α are shown in Figure 6, which proves the validity of the assumption. As shown in Table 3, all the lines are divided into five groups and the strongest line of each group is also

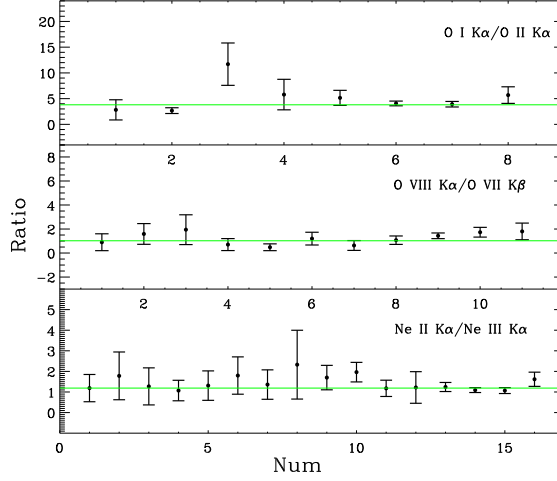


Fig. 6.— The ratio of line strengths between O I $K\alpha$ /O II $K\alpha$, O VIII $K\alpha$ /O VII $K\beta$, as well as Ne II $K\alpha$ /Ne III $K\alpha$. The numbers of observations with both lines are well fitted are: $N(\text{O I } K\alpha/\text{O II } K\alpha) = 8$, $N(\text{O VIII } K\alpha/\text{O VII } K\beta) = 11$, and $N(\text{Ne II } K\alpha/\text{Ne III } K\alpha) = 16$.

found. Then we can use w_i of the five strongest lines of each group to merge the spectra to obtain the wavelength of each line in each group. For the low-ionized O lines, $w_i(\text{O I } K\alpha)$ is used as the weight. $w_i(\text{Mg XI } K\alpha)$ is used as the weight to merge the spectra both for the low-ionized and the high-ionized Mg absorption lines, since the Mg XI $K\alpha$ line is the only Mg absorption line detected significantly.

The co-added spectrum also exhibits very high SNR and we do the same Gaussian fit to every line at neutral, low-ionized, and high-ionized states. The results of neutral or low-ionized, moderate-ionized and high-ionized lines are shown in Table 4.

4. CORRECTION OF THE LINE CENTRAL WAVELENGTHS WITH BAYESIAN ANALYSIS

4.1. Bayesian Analysis

For a sample consisting of N observations, both Methods 1 and 2 merge all the N spectra to a co-added spectrum and can obtain the wavelength by spectral line fitting, but cannot calculate the systematic error. However, we can obtain the line wavelengths (λ_k ; $k = 1, 2, \dots, N$) and errors (σ_k ; $k = 1, 2, \dots, N$) of the N spectra, and then use Bayesian analysis to obtain the 2-D probability distribution of the wavelength (λ_B , hereafter the subscript B denotes the parameter obtained from Bayesian analysis) and the systematic dispersion ($\mathfrak{D}_{\text{sys}}$; note $\mathfrak{D}_{\text{sys}}$ does not include

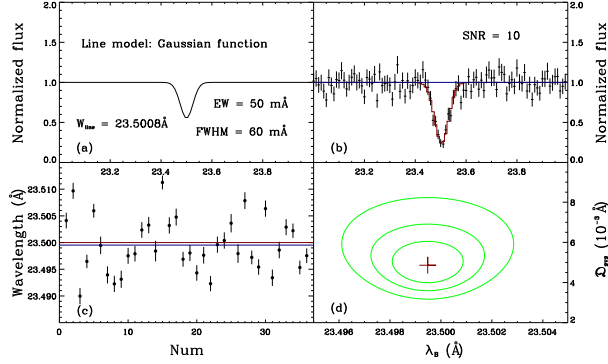


Fig. 7.— The simulation to illustrate how to use Bayesian analysis to obtain λ_B and \mathcal{D}_{sys} . Panel (a) is one of the absorption line model. Panel (b) is the simulated spectrum with the model in panel (a). The absorption line is fitted with a Gaussian function. The distribution of 36 line wavelengths obtained from 36 simulated spectra is shown in Panel (c). The blue and red horizontal lines are the $\bar{\lambda}$ and λ_e of $\Lambda = (\lambda_1, \lambda_2, \dots, \lambda_{36})$ of the 36 simulated spectra. Panel (d) presents the 2-D distribution of λ_B and \mathcal{D}_{sys} that obtained by the Bayesian analysis to the data in Panel (c); the red cross marks the MAP estimates of λ_B and \mathcal{D}_{sys} ; the three contours from the inside out are the 1σ , 2σ , and 3σ credible intervals respectively, which are obtained by calculations over a complete parameter space.

scatter caused by statistical uncertainties). Here we use a 2-D uniform distribution $P(\lambda_B, \mathcal{D}_{\text{sys}})$ as the *a priori* distribution of λ_B and \mathcal{D}_{sys} . According to the Bayesian Theorem, the posterior distribution $P(\lambda_B, \mathcal{D}_{\text{sys}}|\Lambda)$ is given by

$$P(\lambda_B, \mathcal{D}_{\text{sys}}|\Lambda) = \frac{P(\Lambda|\lambda_B, \mathcal{D}_{\text{sys}})P(\lambda_B, \mathcal{D}_{\text{sys}})}{P(\Lambda)} \quad (7)$$

where

$$P(\Lambda|\lambda_B, \mathcal{D}_{\text{sys}}) = \frac{1}{\sqrt{(2\pi)^N}} \prod_{k=1}^N \frac{1}{\sqrt{\mathcal{D}_{\text{sys}}^2 + \sigma_k^2}} e^{-\frac{(\lambda_B - \lambda_k)^2}{2(\mathcal{D}_{\text{sys}}^2 + \sigma_k^2)}}, \quad (8)$$

$$P(\Lambda) = \iint P(\Lambda|\lambda_B, \mathcal{D}_{\text{sys}})P(\lambda_B, \mathcal{D}_{\text{sys}})d\lambda_B d\mathcal{D}_{\text{sys}}, \quad (9)$$

where $\Lambda = (\lambda_1, \lambda_2, \dots, \lambda_N)$ and σ_k ($k = 1, 2, \dots, N$) are the wavelength and its error of each line of these N spectra. Note that when the *a priori* distribution is a 2-D uniform distribution (with unspecified ranges), the Bayesian solution is the same as that obtained from the maximum likelihood estimation. From the 2-D probability distribution, we can obtain the maximum a posteriori (MAP) estimates and errors of λ_B and \mathcal{D}_{sys} . σ_{sys} can be calculated by

$$\sigma_{\text{sys}}^2 = \frac{\mathcal{D}_{\text{sys}}^2}{N}. \quad (10)$$

As shown in Figure 7, in order to illustrate how to use Bayesian analysis to obtain λ_B and \mathcal{D}_{sys} , we make a simulation as follows:

1. Make 36 absorption line models (a normalized continuum plus a Gaussian absorption line) with the line parameters in Table 5. All the continua have spectral wavelength range (23–24 Å) and resolution (0.005 Å). One of the line model is shown in Panel (a).
2. Use the 36 models (step 1) to make 36 simulated spectra. Panel (b) is the simulated spectrum with the model in Panel (a).
3. Fit the 36 simulated spectra with a Gaussian function to obtain 36 simulated line wavelengths (Panel (c)).
4. Use Equations (7-9) to obtain the 2-D probability distribution of λ_B and \mathcal{D}_{sys} (Panel (d)).

From the 2-D probability distribution, we obtain the MAP estimates of λ_B and \mathcal{D}_{sys} (red cross in Panel (c)). The maximum width of the 1σ contour in the X-axis direction is σ_{λ_B} , which is the 1σ error of λ_B . The expectation of the wavelength is $\lambda_e = \hat{\lambda} \pm \hat{\mathcal{D}}/\sqrt{N} = 23.5 \pm 0.00083$ Å. The weighted average of the wavelengths ($\bar{\lambda}$) can be calculated by

$$\bar{\lambda} = \frac{\sum_1^{36} \lambda_k / \sigma_k^2}{\sum_1^{36} 1 / \sigma_k^2}. \quad (11)$$

We have $\bar{\lambda} = 23.49952 \pm 0.00025$ Å and the results from Bayesian analysis are $\lambda_B = 23.49948 \pm 0.00088$ Å and $\mathcal{D}_{\text{sys}} = 0.00494 \pm 0.00066$ Å. In this simple simulation, both $\bar{\lambda}$, λ_B , and \mathcal{D}_{sys} are consistent with the expectation.

4.2. Comparison Between Method 1, Method 2, and Bayesian Analysis

In our work, three methods (Method 1, Method 2, and Bayesian analysis) can be applied to estimate the real wavelengths of the lines from a sample. However, only the strong lines have enough observations with enough SNRs to do the Bayesian analysis. It is very important to know which method can give unbiased results. We answer this question by a simulation as follows:

1. The same as step 1 in Section 4.1, except that both EWs and SNRs of the 36 continua obey a uniform distribution. All the model parameters are sampled once and then fixed as shown in Table 6.
2. Repeat the steps 2–4 in Section 4.1 for 10000 times to obtain the distributions of the results from Method 1, Method 2, and Bayesian analysis (Figure 8).

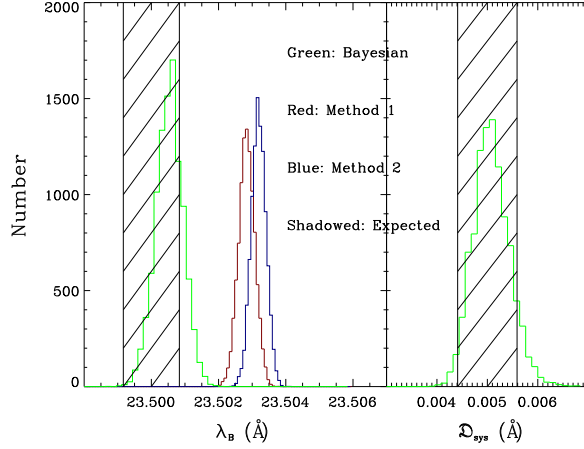


Fig. 8.— Comparison between the result obtained from the co-added spectra fitting (Methods 1 and 2) and Bayesian analysis. In the left panel, the Green histogram is the distribution of λ_B obtained from Bayesian analysis; the red and blue histogram are the distributions of λ_1 and λ_2 obtained from co-added spectrum fitting (Methods 1 and 2); the shadowed region is the 1σ confidence region of λ_e . In the right panel, the Green histogram is the distribution of \mathcal{D}_{sys} obtained from Bayesian analysis; the shadowed region is the 1σ confidence region of \mathcal{D}_e .

In this simulation, the wavelengths of the absorption lines (λ_s ; $s = 1, 2, \dots, N$) in these 36 simulated spectra are set to obey a Gaussian distribution ($\hat{\lambda} = 23.5 \text{ \AA}$, $\hat{\mathcal{D}} = 0.005 \text{ \AA}$), thus the expected value of the mean value of the wavelengths (λ_e) should also obey a Gaussian distribution ($\hat{\lambda}$, $\hat{\mathcal{D}}/\sqrt{N}$), i.e., $23.5 \pm 0.00083 \text{ \AA}$ (The shadowed region in the left panel of Figure 8 is the 1σ confidence region of λ_e). We have $\lambda_1 = 23.50284 \pm 0.00024 \text{ \AA}$ (Method 1; red histogram) and $\lambda_2 = 23.50319 \pm 0.00022 \text{ \AA}$ (Method 2; blue histogram), which are more than 3σ deviations from λ_e . This is because the co-added spectra depend on the spectra with high count-rate (Method 1) or high line-significance (Method 2), which deviate from the expected value of 23.5 \AA significantly. However, the Bayesian analysis gives $\lambda_B = 23.50054 \pm 0.00041 \text{ \AA}$ (green histogram) that is consistent with λ_e . \mathcal{D}_{sys} ($0.00508 \pm 0.00034 \text{ \AA}$) is also consistent with the expected value (\mathcal{D}_e), which obey a Gaussian distribution ($\hat{\mathcal{D}}$, $\hat{\mathcal{D}}/\sqrt{2N}$), i.e., $0.005 \pm 0.00059 \text{ \AA}$ (The shadowed region in the right panel of Figure 8 is the 1σ confidence region of \mathcal{D}_e). Both the errors of λ_1 and λ_2 are smaller than that of λ_B ; we will explain this in Section 4.3. Therefore, co-added spectral fitting can bring biased result, but Bayesian analysis can give unbiased result for both λ_B and \mathcal{D}_{sys} .

4.3. Correction to the Wavelength Obtained from the Co-added Spectra

Since the Bayesian analysis can give unbiased results to both λ_B and \mathcal{D}_{sys} , we can use the results of the Bayesian analysis (λ_B , \mathcal{D}_{sys} , and σ_{λ_B}) to correct the results obtained from the co-added spectra (λ_m and σ_{λ_m} ; $m = 1, 2$ for Methods 1 and 2).

In our statistical model, the unbiased λ_B can be expressed as

$$\lambda_B = \lambda_m + \Delta\lambda_m \pm \sigma_{\text{sys}}, \quad m = 1, 2, \quad (12)$$

where λ_m is the biased result, $\Delta\lambda_m$ is the correction quantity, and σ_{sys} is the systematic error. Thus, σ_{λ_B} can be written as

$$\sigma_{\lambda_B}^2 = \sigma_{\lambda_m}^2 + \sigma_{\Delta\lambda_m}^2 + \sigma_{\text{sys}}^2, \quad m = 1, 2, \quad (13)$$

where σ_{λ_m} and $\sigma_{\Delta\lambda_m}$ are the statistical errors of λ_m and $\Delta\lambda_m$ respectively. For convenience, σ_{λ_m} is the mean value of the asymmetric errors of λ_m in Table 4. As described in Section 4.1, σ_{λ_B} can be obtained from the Bayesian analysis and σ_{sys} can be calculated by Equation (10) from \mathcal{D}_{sys} . From Equations (12) and (13), we can obtain

$$\Delta\lambda_m = \lambda_B - \lambda_m, \quad \text{and} \quad \sigma_{\Delta\lambda_m}^2 = \sigma_{\lambda_B}^2 - \sigma_{\text{sys}}^2 - \sigma_{\lambda_m}^2, \quad m = 1, 2. \quad (14)$$

From the Bayesian analysis, we can extract the statistical component (σ_{stat}) from σ_{λ_B} by

$$\sigma_{\text{stat}}^2 = \sigma_{\lambda_B}^2 - \sigma_{\text{sys}}^2, \quad (15)$$

where σ_{stat} is the total statistical error that consists of both σ_{λ_m} and $\sigma_{\Delta\lambda_m}$ in our model. Therefore, we have $\sigma_{\text{stat}} > \sigma_{\lambda_m}$ and this is why $\sigma_{\lambda_m} < \sigma_{\lambda_B}$ in Section 4.3.

As discussed above, λ_m needs to be corrected as

$$\lambda_{m, c} = \lambda_m + \Delta\lambda_m \pm \sigma_{\text{sys}}, \quad m = 1, 2. \quad (16)$$

$$\sigma_{\lambda_{m, c}}^2 = \sigma_{\lambda_m}^2 + \sigma_{\Delta\lambda_m}^2 + \sigma_{\text{sys}}^2, \quad m = 1, 2. \quad (17)$$

The final errors consist of three parts: statistical error (σ_{λ_m}) from the co-added spectra, statistical error of the correction ($\sigma_{\Delta\lambda_m}$), and systematic error (σ_{sys}) obtained from multi-observations. Because the systematic dispersion of the 36 spectra is partly converted into the broadening of lines in the co-added spectrum, σ_{λ_m} also partially includes σ_{sys} . Therefore, $\sigma_{\lambda_{m, c}}$ is the conservative estimate of the final total error.

4.4. Application of Bayesian Analysis to Our Sample

Although the co-added spectrum has extremely high SNR that can help us to find some weak lines, it can bias towards the observations with high count-rate (Method 1) or high line-significance

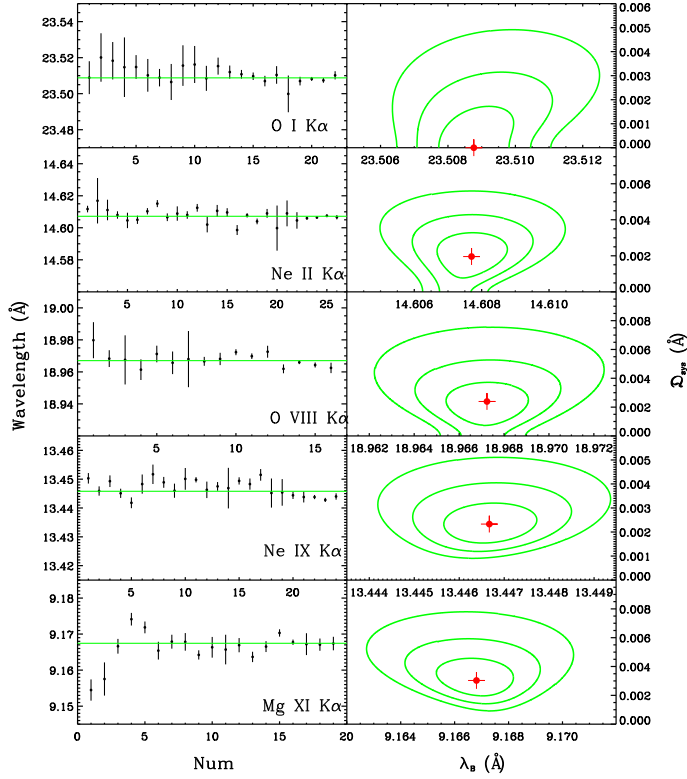


Fig. 9.— Distributions of the wavelengths of O I K α , Ne II K α , O VIII K α , Ne IX K α , and Mg XI K α obtained from all the well-fitted observations. The contours and the red crosses in the right panels are the same as in Figure 7.

(Method 2). Bayesian analysis can obtain the unbiased result; however, only the strong lines have enough observations with enough SNRs to do the Bayesian analysis.

As shown in Table 3, all the lines have been divided into five groups and the strongest line of each group is also found. Since the absorption clouds within each group are assumed to have the same velocities, we can obtain the unbiased result for all the lines as follows: (1) use Methods 1 and 2 to obtain the results of high SNR co-added spectra; (2) use the results of Bayesian analysis of the strongest line of each group to correct all other lines in the same group, e.g., $\Delta\lambda_m(\text{O I K}\alpha)$ is used to correct the low-ionized O lines; see Tables 3, 7 and Figure 9 for details. The final results are shown in Tables 8–10.

The Mg XI K α line is very special. We find that for the Mg XI K α line $\sigma_{\text{sys}} > \sigma_{\text{stat}}$. This means that, unlike O VIII K α and Ne IX K α , $\sigma_{\lambda_{1,2}}$ of the Mg XI K α lines is not dominated by statistical error, but by the components caused by the line broadening when a co-added spectrum is produced, i.e., σ_{sys} increases σ_{λ_m} significantly. $\Delta\lambda_m$ of the Mg XI K α line in Table 7 is very uncertain and

we cannot obtain $\sigma_{\Delta\lambda_m}$ with Equation (14). In order to correct the wavelength of the Mg lines, we must make an assumption that the motion of both the low-ionized and the high-ionized Mg are the same as that of Ne. Thus we can use $\Delta\lambda_m(\text{Ne II K}\alpha)$ to correct the low-ionized Mg lines and use $\Delta\lambda_m(\text{Ne IX K}\alpha)$ to correct the moderate-ionized and high-ionized Mg lines respectively.

For the Fe 2d-3p double lines, we also use $\Delta\lambda_m(\text{Ne IX K}\alpha)$ to correct the value obtained from the co-added spectra (Methods 1 and 2; Table 4).

5. DISCUSSION

5.1. The Two Methods of Merging the Spectra

In the Section 3, two different methods are used to merge all the 36 observations. Method 1 is very simple: we only need to add the counts of each spectrum channel by channel, i.e., every spectrum has the same weight. However, Method 1 implicitly assumes that all the spectra have the same absorption column densities, i.e., the same weight. When we merge two spectra that one has a strong absorption line (e.g., the O VI K α in ObsId 6618) and the other has a weak absorption line (e.g., the O VI K α in ObsId 8599), the spectrum with weak absorption line can dilute or even wipe out the absorption line in the co-added spectrum, i.e., reduce the significance of the absorption line. To avoid this problem, we use the significance of the absorption line as the weight to merge the spectra instead (Method 2). The spectra that only contribute to the continuum are abandoned in this method, since the continuum is actually the noise for the absorption lines. From Table 4, we can see that the results obtained by the two methods are consistent with each other for most of the absorption lines, except for some weak lines (e.g., O III K α) that are too weak to be fit with a Gaussian function. In addition, several suspicious lines may be faked, as they are only present in the co-added spectrum of Method 1 (Mg IV K α and Ne IV K α). The significance levels of the lines in the co-added spectrum obtained with Method 2 are not remarkably higher than that obtained with Method 1. This means that the assumptions of both Methods 1 and 2 are reasonable for our sample. More high-quality observations of more targets are the key to the determination of the wavelength of these weak transitions.

5.2. Systematic Errors of the Lines in Co-added Spectra

As described in Section 4.2, although both Methods 1 and 2 can obtain the spectra with high SNRs, however, both λ_1 and λ_2 are biased. In addition, σ_{λ_1} and σ_{λ_2} are smaller than the true value, because σ_{sys} is not considered. In this sub-section, we emphasize another important source of σ_{sys} ,

i.e., σ_{sys} caused by the uncertainty of the spectral fitting.

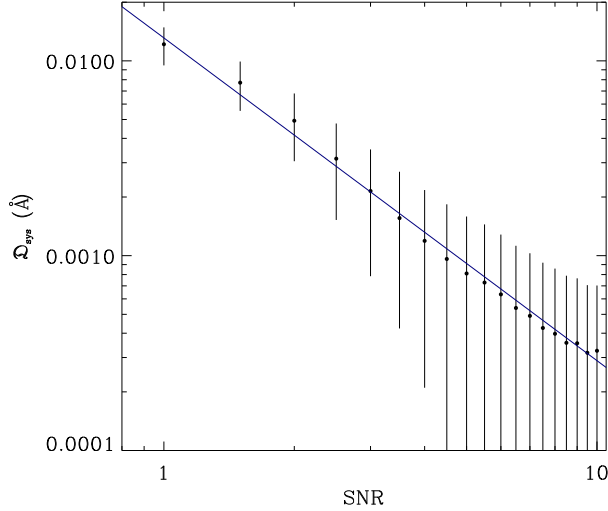


Fig. 10.— The dependence of \mathcal{D}_{sys} on the SNRs of the spectra.

The SNRs of some observations are so low that the fluctuations of the continua will seriously affect the fitting result of the weak lines. We can quantify this uncertainty with simulation. In this simulation, we take the SNR of the simulated spectrum as the only variable to test the dependence of the systematic uncertainty on the SNRs of the spectra. The SNR range is between 1 and 10, with a step of 0.5, as shown in Figure 10. For each SNR, we make the simulation as follows:

1. The same as step 1 in Section 4.1, except that the line central wavelength is fixed at 23.5 \AA .
2. Repeat the steps 2–4 in Section 4.1 10000 times to obtain λ_{B} and the error of the \mathcal{D}_{sys} .

Finally, for each SNR, we obtain \mathcal{D}_{sys} and its error, as shown in Figure 10. We find that \mathcal{D}_{sys} increases dramatically as the SNR decreases. The relationship between the SNR and \mathcal{D}_{sys} is similar to the form of a power-law. The reason for this anti-correlation is that the error propagation of the Gaussian fitting is nonlinear when the statistical error is large. Therefore, the joint analysis of all the observations can reduce the systematic uncertainty due to the improvement of the SNRs of the co-added spectra.

σ_{sys} can be caused by other uncertainties, such as the imprecise Galactic rotation correction that depends on several uncertain models (e.g., the distribution of the gas inside and above the Galactic Plane). Because the parameters of the Galactic rotation model are still uncertain, we cannot give accurate value of systematic uncertainty caused by this uncertainty. Nevertheless, the total systematic uncertainty can be obtained from the distribution of the lines of the 36 observations, as

described in Section 4.1. Due to the limitation of the SNRs, we cannot do Bayesian analysis to all the lines. However, since the absorption clouds with the similar degree of ionization are assumed to have the same velocities as shown in Table 3, we use σ_{sys} of the strongest line to represent the systematic uncertainty of all the lines in the same group, e.g., $\sigma_{\text{sys}}(\text{Ne II K}\alpha)$ represents the systematic uncertainty of the low-ionized Ne lines.

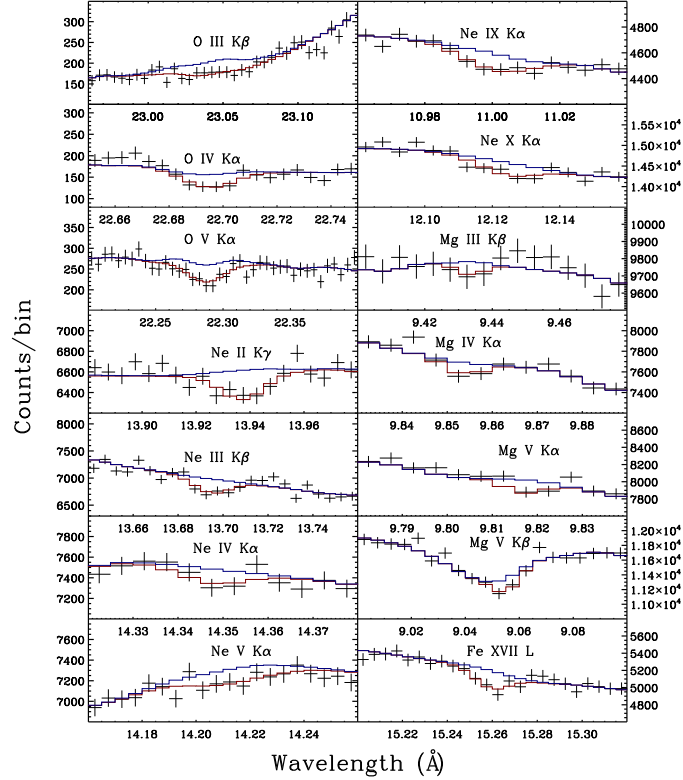


Fig. 11.— All the lines with $snr_1 < 5$ in Table 4.

5.3. Detection of the K Transitions in Soft X-ray Band

As described above, our results on the wavelengths of K transitions of high-ionized O, Ne, and Mg are the most accurate so far, because more sources are used to reduce the systematic uncertainty induced by the Galactic rotation correction and more observations are used to reduce the statistical error. Our results are also unbiased, because we do the bias correction for each line. Among all the lines, Ne IX K α is the most accurate, with an error of only 0.7 m \AA , which is equivalent to about 14 km s $^{-1}$. This error is so small that it may be used to measure the low-velocity gas, e.g., the hot high-ionized gas in Galactic halo. For the lines whose wavelengths are consistent between NIST and V96, our results are also consistent with those. For those lines whose wavelengths are inconsistent

between NIST and V96, our results are closer to that in NIST. Compared to Y09, our results are two times more accurate (e.g., O VIII K α) and are also consistent with theoretical calculations except the O VII K α and the Ne X K α lines (Table 10). In our work, $\lambda_{\text{m}}(\text{Ne X K}\alpha) = 12.1264_{-3.4}^{+2.6}$ Å is 7.5 mÅ lower than the value of 12.1339 Å in V96. We note that NIST does not include this line. The O VII K α line is more complicated and it is also 10 mÅ lower than that in NIST and V96. We will discuss this in the next sub-section.

Unlike the high-ionized elements, in the soft X-ray band, there still exists large discrepancies between the astronomical observations and the theoretical calculations of K transitions of the low-ionized and moderate-ionized elements (Table 1). In fact, some of these lines (e.g., 1s–3p of Mg III and 1s–2p of Mg IV) have even never been detected. The co-added spectra have excellent SNRs that provides us an unique opportunity to detect these weak absorption lines. We are particularly concerned about these transitions and thus search for the signals of these absorption lines around their theoretical values. For the 11 transitions of the low-ionized elements shown in Table 8, $N_{\text{snr}_1 > 5} = 7$ and $N_{3 < \text{snr}_1 < 5} = 3$. Only $\text{snr}_1(\text{Mg III K}\alpha) < 3$, but $\text{snr}_2(\text{Mg III K}\alpha) > 3$. Despite the low SNRs, it is the first detection of the Mg III K α line so far. Several moderate-ionized ions, i.e., the O, Ne, and Mg lines shown in Table 9 (except the O VI K α that has been detected in Y09), also appear for the first time around the theoretical values in the co-added spectra. As shown in Table 9, only $\text{snr}_1(\text{O VI K}\alpha \text{ and Ne VII K}\alpha) > 5$. However, among the other lines, $\text{snr}_1(\text{Ne IV K}\alpha \text{ and Mg IV K}\alpha) \leq 3$. Moreover, the Ne IV K α and Mg IV K α lines are only present in the co-added spectrum of Method 1, which hints that these three lines may be artificial and need to be confirmed by higher quality observations in the future.

In Y09, only one of the 2d-3p double lines, i.e., the Fe XVII 15.01 Å line was detected, but no statistical error was given. In our work, both Fe XVII 15.01 Å and 15.26 Å lines are detected significantly for the first time simultaneously (Figures 3 and 4; Table 9). All the lines with $\text{snr}_1 < 5$ are shown in Figure 11.

5.4. Wavelength of the O VII K α Lines

By analyzing the co-add spectrum, the wavelengths of all the strong absorption lines can be determined accurately. In our work, several O VII lines, including even the very weak O VII K γ , are found. However, the wavelength of O VII K α is still uncertain. The observations of Cyg X–2 and XTE J1817–330 are the most important components of the co-added spectrum, which have enough counts and thus can greatly determine the shape of the co-added spectrum. Y09 jointly analyzed four *Chandra*-HETG observations of Cyg X–2 and found the O VII K β line clearly but no O VII K α line was detected. This problem can be interpreted by an unknown emission that fills in the absorption (Cabot et al. 2013). The spectrum of XTE J1817–330 is similar to Cyg X–2

but more complex, which can be caused by not only two absorption lines but also an absorption line plus an emission line. Thus, the co-added spectrum can also be well fitted by two different models (Figure 12). For the model of a strong absorption line plus a weak redshifted absorption line, the fitting value of the O VII K α line is 21.5915 ± 0.0015 Å. However, for the model of an absorption line plus a weak emission line, the fitting value is 21.6074 ± 0.0015 Å. Both values are very different from the theoretical value of 21.6020 Å given by NIST or 21.6019 Å given by V96. We cannot distinguish which model is correct due to the limitation of the SNR of the spectrum.

6. SUMMARY

So far, the wavelengths of K alpha absorption lines of neutral, low-ionized, and moderate-ionized O, Ne, and Mg have not been determined precisely, either in theoretical calculations (e.g., V96; NIST), laboratory measurements (Stolte et al. 1997), or in astronomical observations (J0406; Y09). In order to obtain the wavelengths of K transitions of O, Ne, and Mg more accurately, we jointly analyzed 36 *Chandra*-HETG observations of 11 LMXBs at low Galactic latitudes in this work. We corrected the Galactic rotation velocity to the rest frame for every observation and then used two different methods to merge all the corrected spectra to a co-added spectrum. Finally, we fit and obtained the wavelengths of every absorption line in the co-added spectrum obtained by the above two methods (Section 3). Both methods give similar and consistent results for most lines, as shown in Figure 3.

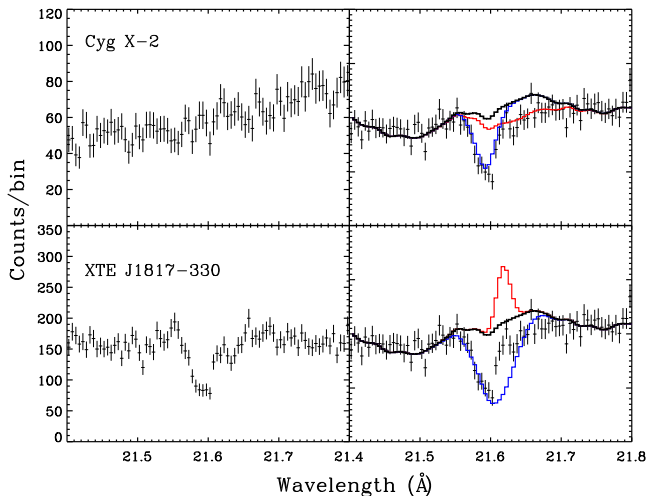


Fig. 12.— The left two panels are the co-added spectra around O VII K α of Cyg X–2 and XTE J1817–300 respectively. The line fitting of the final co-added spectrum with two different models (upper: absorption + absorption; lower: absorption + emission) are shown in the right panels.

We noted that the co-added spectra obtained by the usual methods (Methods 1 and 2) exhibit biases, which are very important for the calibration of the lines. The co-added spectrum can be biased to the observations of high counts (Method 1) or high SNRs of the lines (Method 2). We made Bayesian analysis to the lines of the O I $K\alpha$, Ne II $K\alpha$, O VIII $K\alpha$, Ne IX $K\alpha$ to obtain the systematic uncertainty and the bias correction of the O, Ne, and Mg lines in all phases. The final results after the bias correction are summarized as follows:

(1) For the the neutral, low-ionized, and high-ionized lines, the accuracy of our result is five and two times higher than J0406 and Y09 respectively (Table 4). Several lines that were not detected (i.e., O III $K\alpha$, Ne II $K\gamma$, Mg III $K\beta$, and Ne IX $K\gamma$) or too weak to give measurement errors (i.e., O I $K\beta$, O VII $K\gamma$ and Ne X $K\alpha$) in Y09 are detected clearly in our work. We also find the moderate-ionized lines of these elements (O IV $K\alpha$, O V $K\alpha$, Ne IV $K\alpha$, Ne V $K\alpha$, Ne VII $K\alpha$, Mg IV $K\alpha$, Mg V $K\alpha$, and Mg V $K\beta$; Table 9) whose significances are so low that need to be confirmed in the future. Besides the remarkable improvement of the accuracy, it is worth mentioning that all the biases measurements here are corrected (Tables 8–10).

(2) The systematic uncertainty in our measurement mainly comes from the Galactic rotation correction and the spectral fitting. The former depends on the Galactic model. For the latter, we make simulations to estimate the effect. The total systematic uncertainties are: $\sigma_{\text{sys}} = 0 \text{ m}\text{\AA}$ and $0.6 \text{ m}\text{\AA}$ for low-ionized and high-ionized O, $\sigma_{\text{sys}} = 0.4 \text{ m}\text{\AA}$ and $0.5 \text{ m}\text{\AA}$ for low-ionized and high-ionized Ne, $\sigma_{\text{sys}} = 0.7 \text{ m}\text{\AA}$ for Mg lines (Table 7).

(3) For high-ionized lines of O VII $K\beta$ and O VIII $K\alpha$, our results are consistent with that of NIST, but $2 \text{ m}\text{\AA}$ lower than V96. For Ne X $K\alpha$, our result is about $8 \text{ m}\text{\AA}$ lower than that given by V96; NIST does not provide the theoretical value. For the moderate-ionized lines, the discrepancy between our measurements and the theoretical calculations are generally between 1 to $80 \text{ m}\text{\AA}$. Because the statistical errors of these lines are also similar to the discrepancy, the measurements are consistent with the theoretical calculations.

JYL thanks Dr. Yuan Liu for helping on improving the draft manuscript. SNZ acknowledges partial funding support by 973 Program of China under grant 2009CB824800, and by the National Natural Science Foundation of China under grant Nos. 11133002, 10821061, and 10725313.

APPENDICES

A. The relationship between the absorption column density (N_{H}) and the error of the wavelength of the absorption line (σ_{λ})

For the spectrum with a continuum plus a Gaussian absorption line, the wavelength of the line center (λ) can be determined by line fitting with a Gaussian function

$$\phi(\lambda_i) = d e^{-\frac{(\lambda_i - \lambda)^2}{2b^2}}, \quad (\text{A1})$$

where d , b , and λ are the depth, broadening, and center wavelength of the line. As described in Landman et al. (1982) and Lenz & Ayres (1992), σ_{λ} (the error of λ) can be expressed as

$$\sigma_{\lambda}^2 \propto \frac{\sigma^2 b}{d^2}, \quad (\text{A2})$$

where σ is the error of the continuum around the line. For an observed spectrum, if the observation time is fixed, σ^2 and d can be expressed as

$$\sigma^2 \propto f \propto e^{-\tau_c}, \tau_c = \sigma_c N_{\text{H}}, \quad (\text{A3})$$

and

$$d \propto f \cdot (1 - e^{-\tau_1}) \propto e^{-\tau_c} (1 - e^{-\tau_1}), \tau_1 = \sigma_1 f_i N_{\text{H}}, \quad (\text{A4})$$

where f is the flux of the continuum, τ_c and τ_1 are the optical depths of the continuum and the line center, σ_c and σ_1 are the cross sections for the continuum and the line center, and f_i is the abundance of the ion producing the absorption line. Thus σ_{λ}^2 can be written as

$$\sigma_{\lambda}^2 \propto \frac{1}{e^{-\sigma_c N_{\text{H}}} (1 - e^{-\sigma_1 f_i N_{\text{H}}})^2}. \quad (\text{A5})$$

We use the observation of the O VIII K α line in Y09 to show the relationship between N_{H} and σ_{λ} . Here $\sigma_c = 5.9 \times 10^{-22} \text{cm}^2$ is obtained from Morrison & McCammon (1983) and $\sigma_1 f_i = 1.1 \times 10^{-22} \text{cm}^2$ is calculated from the observation in Y09. As shown in Figure 13, for either too low or too high N_{H} the error of the O VIII K α can be increased significantly.

B. The weights of the absorption lines to merge to a co-added spectrum.

In Equation (A2), d can also be described by $d \propto \frac{a}{b}$, where a is the normalization of the line. Thus we have

$$\sigma_{\lambda}^2 \propto \frac{\sigma^2 b^3}{a^2}. \quad (\text{B1})$$

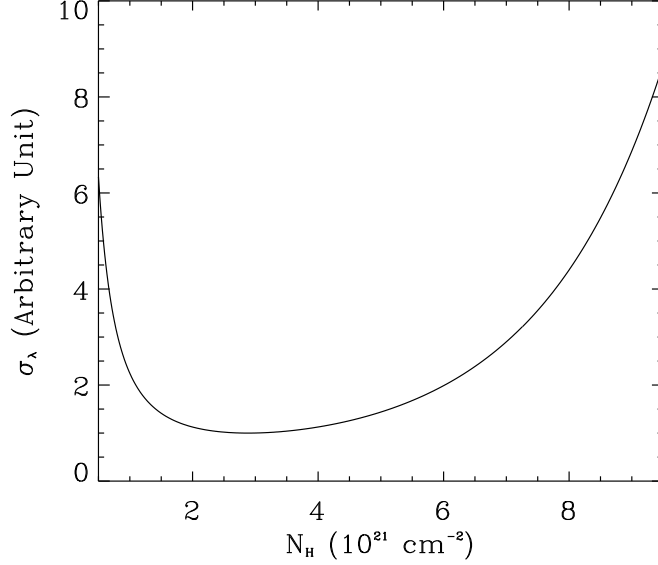


Fig. 13.— The relationship between the absorption column density (N_H) and the error of the wavelength of the absorption line (σ_λ). The lowest point of the curve is normalized to 1.

When merging two spectra with the same absorption lines with weights w_1 and w_2 , we have

$$\sigma'^2 = \sigma_1^2 w_1^2 + \sigma_2^2 w_2^2 \quad (\text{B2})$$

$$a' = a_1 w_1 + a_2 w_2 \quad (\text{B3})$$

$$d' = d_1 w_1 + d_2 w_2 \propto \frac{a_1}{b_1} w_1 + \frac{a_2}{b_2} w_2 \quad (\text{B4})$$

$$b' \propto \frac{a'}{d'} \propto \frac{a_1 w_1 + a_2 w_2}{\frac{a_1}{b_1} w_1 + \frac{a_2}{b_2} w_2}. \quad (\text{B5})$$

where superscript ‘ \prime ’ refers to the parameters of the co-add spectra. Thus $\sigma'_\lambda{}^2$ can be expressed as

$$\sigma'_\lambda{}^2 \propto \frac{\sigma'^2 b'^3}{a'^2} \propto (\sigma_1^2 w_1^2 + \sigma_2^2 w_2^2) \frac{a_1 w_1 + a_2 w_2}{\left(\frac{a_1}{b_1} w_1 + \frac{a_2}{b_2} w_2\right)^3}. \quad (\text{B6})$$

Defining $k = \frac{w_1}{w_2}$, $m = \frac{a_1}{a_2}$, and $n = \frac{b_1}{b_2}$, we then have

$$\sigma'_\lambda{}^2 \propto (\sigma_1^2 k^2 + \sigma_2^2) \frac{mk + 1}{\left(\frac{m}{n}k + 1\right)^3}. \quad (\text{B7})$$

Usually the absorption lines to be merged usually have a similar broadening, i.e., $n \sim 1$, as exemplified in Figure 14. Therefore, the above equation can be simplified as

$$\sigma'_\lambda{}^2 \propto (\sigma_1^2 k^2 + \sigma_2^2) \frac{1}{\left(\frac{m}{n}k + 1\right)^2}. \quad (\text{B8})$$

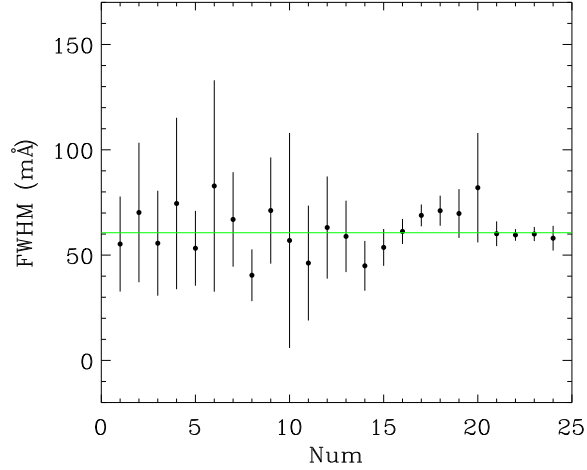


Fig. 14.— The distribution of the observed Gaussian broadening b of the O I $K\alpha$ line. Here only the line fitting results with $\sigma_b < 30 \text{ m}\text{\AA}$ are plotted, which are consistent with the same value.

We can obtain that the value of k for minimum $\sigma'_\lambda{}^2$ as

$$k = \frac{\sigma_2^2 m}{\sigma_1^2 n} = \frac{a_1}{\sigma_1^2 b_1} / \frac{a_2}{\sigma_2^2 b_2}, \quad (\text{B9})$$

i.e., the weight of each line can be expressed as

$$w_i = \frac{a_i}{\sigma_i^2 b_i}. \quad (\text{B10})$$

Therefore, we adopt Equation (B10) as the weight of each line to merge all data to a co-added spectrum.

REFERENCES

- Behar, E., & Netzer, H. 2002, *ApJ*, 570, 165
- Bowen, D. V., et al. 2008, *ApJS*, 176, 59
- Cabot S. H., Wang, D. Q., & Yao, Y. 2013, *MNRAS*, 431, 511
- Dewey, D., Zhekov, S. A., McCray, R., & Canizares, C. R. 2008, *ApJ*, 676, L131
- Fang, T. T., Sembach, K. R., Canizares, C. R. 2003, *ApJ*, 586, L49
- Galloway, D. K., Munro, M. P., Hartman, J. M., Psaltis, D., & Chakrabarty, D. 2008a, *ApJS*, 179,

- García, J., Mendoza, C., Bautista, M. A., Gorczyca, T. W., Kallman, T. R., Palmeri, P. 2005, *ApJ*, 158, 68
- Gorczyca, T. 2000, *Phys. Rev. A.*, 61, 024702
- Gorczyca, T., & McLaughlin, B. 2005, *BAPS*, 50, 39
- Iaria, R., et al. 2004, *ApJ*, 600, 358
- Juett, A. M., Schulz, N. S., & Chakrabarty, D. 2004, *ApJ*, 612, 308
- Juett, A. M., Schulz, N. S., Chakrabarty, D., & Gorczyca, T. W. 2006, *ApJ*, 648, 1066
- Juett, A. M., & Chakrabarty, D. 2006, *ApJ*, 646, 493
- Kalberla, P. M. W., et al. 2005, *å*, 440, 775
- Kallman, T. R., Palmeri, P., Bautista, M. A., Mendoza, C., & Krolik, J. H. 2004, *ApJS*, 155, 675
- Kong, A. K. H., Charles, P. A., Homer, L., Kuulkers, E., & O'Donoghue, D. 2006, *MNRAS*, 368, 781
- Kuulkers, E., et al. 2010, *å*, 514, A65
- Landman, D. A., Robert, R. D., Tanigawa, G. 1982, *ApJ*, 261, 732
- Lee, J. C., et al. 2001, *ApJ*, 554, L13
- Lenz, D. D., & Ayres, T. R. 1992, *PASP*, 104, 1104
- Miller, J. M., et al. 2004, *ApJ*, 601, 450
- Miller, J. M., et al. 2006, *Nature*, 441, 953
- Morrison, R., & McCammon, D. 1983, *ApJ*, 270, 119
- Nicastro, F., et al. 2005, *ApJ*, 629, 700
- Rand, R. J. 1997, *ApJ*, 474, 129
- Rand, R. J. 2000, *ApJ*, 537, L13
- Raassen, A. J. J., Ness, J. U., Mewe, R., van der Meer, R. L. J., Burwitz, V., & Kaastra, J. S. 2003, *å*, 400, 671
- Sala, G., Greiner, J., Bottacini, E., & Haberl, F. 2007, *Ap&SS*, 309, 315

- Schattenburg, M. L., & Canizares, C. R. 1986, ApJ, 301, 759
- Schulz, N. S., et al. 2002, ApJ, 565, 1141
- Smith, R. K., Brickhouse, N. S., Liedahl, D. A., & Raymond, J. C. 2001, ApJ, 556, L91
- Sparke, L. S., & Gallagher, J. S. 2000, Galaxies in the Universe: an Introduction, Cambridge University Press
- Steenbrugge, K. C., Kaastra, J. S., de Vries, C. P., & Edelson, R. 2003, *Å*, 402, 477
- Stolte, W. C., et al. 1997, J. Phys. B, 30, 4489
- Verner, D. A., Verner, E. M., & Ferland, G. J. 1996, ADNDT, 64, 1
- Yao, Y., & Wang, Q, D. 2005, ApJ, 624, 751
- Yao, Y., Nowak, M. A., Wang, Q. D., Schulz, N. S., & Canizares, C. R. 2008, ApJ, 672, L21
- Yao, Y., Schulz, N. S., Gu, M. F., Nowak, M. A. & Canizares, C. R. 2009, ApJ, 696, 1418

Table 3. Five different line groups with different ionized states and different elements

	O (L)	O (M & H)	Ne (L)	Ne (M & H)	Mg (A)
strongest	O I $K\alpha$	O VIII $K\alpha$	Ne II $K\alpha$	Ne IX $K\alpha$	Mg XI $K\alpha$
1s–2p	O I, O II, O III	O IV, O V, O VI, O VII, O VIII	Ne II, Ne III	Ne IV, Ne V, Ne VII, Ne IX, Ne X	Mg IV, Mg V, Mg XI
1s–3p	O I	O VII, O VIII	Ne I, Ne II, Ne III	Ne IX	Mg III, Mg V
1s–4p		O VII	Ne II	Ne IX	

Note. — The 1st row are the group names, where ‘L’, ‘M’, and ‘H’ means the low-ionized, moderate-ionized, and high-ionized state. ‘A’ means all ionized states. The 2nd row lists the strongest lines in each group.

Table 4. The wavelengths of low-ionized, moderate-ionized, and high-ionized elements

Ion	Transition	$\lambda_1(\text{\AA})$	snr_1	$\lambda_2(\text{\AA})$	snr_2
O I	1s–2p	23.5087 ^{+0.6} _{-0.6}	49.9	23.5091 ^{+0.7} _{-0.7}	44.1
O I	1s–3p	22.8834 ^{+2.3} _{-2.3}	5.5	22.8872 ^{+2.4} _{-2.3}	3.1
O II	1s–2p	23.3508 ^{+1.3} _{-0.9}	14.2	23.3507 ^{+1.1} _{-1.1}	13.4
O III	1s–2p	23.0392 ^{+8.5} _{-5.4}	4.2	23.0565 ^{+7.1} _{-8.3}	2.4
O IV	1s–2p	22.6969 ^{+2.9} _{-37.3}	4.1	22.6967 ^{+3.4} _{-3.3}	2.9
O V	1s–2p	22.2849 ^{+4.7} _{-3.3}	4.4	22.2872 ^{+3.0} _{-4.2}	3.1
O VI	1s–2p	22.0281 ^{+2.5} _{-1.4}	6.3	22.0292 ^{+1.5} _{-2.2}	7.4
O VII	1s–2p	21.5915 ^{+1.6} _{-1.3}	7.1	21.5948 ^{+1.4} _{-1.5}	10.6
O VII	1s–3p	18.6259 ^{+1.1} _{-0.7}	13.0	18.6255 ^{+1.1} _{-0.9}	10.9
O VII	1s–4p	17.7657 ^{+0.9} _{-1.2}	9.5	17.7673 ^{+0.8} _{-1.3}	6.1
O VIII	1s–2p	18.9667 ^{+0.5} _{-0.9}	18.1	18.9664 ^{+0.8} _{-0.7}	16.3
O VIII	1s–3p	16.0046 ^{+0.6} _{-1.3}	8.3	16.0044 ^{+1.3} _{-1.3}	8.2
Ne I	1s–3p	14.2937 ^{+0.9} _{-2.9}	7.8	14.2942 ^{+0.7} _{-0.7}	10.7
Ne II	1s–2p	14.6068 ^{+0.4} _{-0.3}	29.4	14.6071 ^{+0.4} _{-0.4}	28.0
Ne II	1s–3p	14.0029 ^{+1.0} _{-0.7}	11.6	14.0031 ^{+0.9} _{-0.9}	11.3
Ne II	1s–4p	13.9373 ^{+1.5} _{-3.0}	4.5	13.9339 ^{+3.2} _{-2.9}	4.5
Ne III	1s–2p	14.5068 ^{+0.7} _{-0.6}	15.0	14.5073 ^{+0.7} _{-0.7}	18.1
Ne III	1s–3p	13.6951 ^{+1.4} _{-2.4}	3.8	13.6953 ^{+1.7} _{-2.5}	5.1
Ne IV	1s–2p	14.3471 ^{+64.3} _{-64.3}	1.8
Ne V	1s–2p	14.2127 ^{+10.2} _{-38.6}	3.2	14.2090 ^{+12.6} _{-13.7}	2.2
Ne VII	1s–2p	13.8272 ^{+4.2} _{-1.9}	5.3	13.8269 ^{+3.3} _{-4.2}	3.2
Ne IX	1s–2p	13.4455 ^{+0.5} _{-0.3}	27.6	13.4453 ^{+0.4} _{-0.4}	26.1
Ne IX	1s–3p	11.5459 ^{+1.4} _{-0.7}	11.0	11.5456 ^{+1.6} _{-1.0}	9.9
Ne IX	1s–4p	11.0010 ^{+2.5} _{-2.5}	4.1	10.9987 ^{+1.9} _{-1.8}	2.6
Ne X	1s–2p	12.1250 ^{+2.1} _{-4.1}	3.4	12.1253 ^{+2.9} _{-2.4}	3.8
Mg III	1s–3p	9.4330 ^{+44.8} _{-22.1}	1.5	9.4766 ^{+0.6} _{-4.1}	3.2
Mg IV	1s–2p	9.8539 ^{+29.1} _{-1.0}	1.5
Mg V	1s–2p	9.8191 ^{+30.1} _{-30.1}	3.3	9.8195 ^{+1.4} _{-1.9}	1.0
Mg V	1s–3p	9.0569 ^{+28.0} _{-2.0}	3.0	9.0553 ^{+2.5} _{-1.9}	2.3
Mg XI	1s–2p	9.1679 ^{+0.6} _{-0.7}	9.7	9.1679 ^{+0.6} _{-0.7}	9.5
Fe XVII	2p–3d	15.0124 ^{+1.9} _{-1.6}	8.6	15.0123 ^{+0.8} _{-0.9}	7.5
Fe XVII	2p–3d	15.2596 ^{+1.0} _{-4.2}	4.7	15.2612 ^{+1.9} _{-2.6}	3.7

Note. — λ_i and snr_i ($i = 1, 2$) are the wavelength and signal to noise ratio of the absorption lines from Methods 1 and 2. $snr_1 = EW/\sigma_{EW}$ and $snr_2 = a/\sigma_a$, where EW is the equivalent width and a is the normalization of Gaussian-fit lines. All the errors are in units of mÅ and at 1σ levels.

Table 5. Line parameters of the simulation in Section 4.1

Wavelength (Å)	FWHM (mÅ)	EW (mÅ)	SNR
$(\hat{\lambda} = 23.5, \hat{\mathcal{D}} = 0.005)$	60	50	10

Note. — The wavelength obey a Gaussian distribution ($\hat{\lambda}$, $\hat{\mathcal{D}}$) and the other parameters are constant.

Table 6. Line parameters of the simulation in Section 4.2

λ_s (Å)	EW (mÅ)	SNR	λ_s (Å)	EW (mÅ)	SNR
23.5053	20.9	28.9	23.4995	14.9	11.2
23.5091	49.9	29.7	23.4944	38.0	22.3
23.4916	33.3	9.1	23.4970	26.7	15.3
23.4967	34.7	12.7	23.4926	16.6	8.7
23.5092	14.2	16.1	23.5016	49.3	25.3
23.5002	23.2	14.7	23.5008	40.5	22.4
23.4950	20.0	9.4	23.5023	47.9	22.9
23.4959	31.7	9.8	23.4959	26.9	17.4
23.4934	49.6	9.2	23.5090	44.7	28.5
23.4987	22.3	10.2	23.5002	28.3	8.9
23.5001	35.2	12.4	23.4950	29.4	18.7
23.5037	31.4	23.0	23.5076	18.2	23.7
23.5020	17.8	20.5	23.4957	21.8	17.1
23.5003	22.0	26.3	23.4990	44.9	5.8
23.5116	33.4	25.8	23.5022	31.3	24.3
23.5033	45.3	17.2	23.5002	27.6	20.3
23.5044	33.4	24.3	23.4998	20.6	7.2
23.4961	28.3	7.7	23.4971	40.8	18.7

Note. — λ_s (Gaussian distribution; $\hat{\lambda} = 23.5$ Å, $\hat{\sigma} = 0.005$ Å), EWs (uniform distribution; 10-50 mÅ), and SNRs (uniform distribution; 5-30).

Table 7. Comparison between the Bayesian analysis and the co-added spectrum fitting of the strong lines O I, O VIII, Ne II, Ne IX, and Mg XI

Ion	Transtion	λ_B	σ_{λ_B}	σ_{sys}	σ_{stat}	$\Delta\lambda_1$	$\Delta\lambda_2$	$\lambda_{i, c} (i = 1, 2)$
O I	1s–2p	23.5088	0.8	0.0	0.8	+0.1(0.5)	–0.3(0.3)	O (L)
O VIII	1s–2p	18.9676	1.1	0.6	1.0	+0.6(0.6)	+0.8(0.6)	O (M & H)
Ne II	1s–2p	14.6076	0.7	0.4	0.5	+0.9(0.4)	+0.6(0.4)	Ne (L) & Mg(L)
Ne IX	1s–2p	13.4465	0.7	0.5	0.5	+1.1(0.3)	+1.3(0.3)	Ne (M & H) & Mg (M & H)
Mg XI	1s–2p	9.1670	0.9	0.7	0.6	–0.8(*)	–0.9(*)	* * * *

Note. — λ_B , σ_{λ_B} , and σ_{sys} are obtained from the Bayesian analysis in Figure 9. λ_B is in units of Å and all the other data are in units of mÅ. All the errors in parentheses are at 1σ levels. σ_{stat} is calculated with Equation (15). $\Delta\lambda_1$ and $\Delta\lambda_2$, as well as their errors, are calculated with Equation (14). ‘*’ means that we cannot obtain $\sigma_{\Delta\lambda_i}$ because σ_{stat} is smaller than σ_i in Table 4. The last column lists the lines to be corrected and ‘L’, ‘M’ and ‘H’ are the same as that defined in Table 3. Please see Section 4.3 for details.

Table 8. Comparison of the wavelengths of low-ionized elements between the corrected values in this paper, observations in Y09, and the theoretical calculations.

Ion	Transtion	$\lambda_{1, c}(\text{\AA})$	$\lambda_{2, c}(\text{\AA})$	$\lambda_m(\text{\AA})$	Y09(\AA)	G05BN02(\AA)	G00GM05(\AA)
O I	1s–2p	23.5088 ^{+0.8} _{-0.8}	23.5088 ^{+0.8} _{-0.8}	23.5088 ^{+0.8} _{-0.8}	23.508 ^{+1.6} _{-1.6}	23.4475	23.532
O I	1s–3p	22.8834 ^{+2.4} _{-2.4}	22.8869 ^{+2.4} _{-2.3}	22.8852 ^{+2.4} _{-2.4}	22.886(<i>f</i>)	...	22.907
O II	1s–2p	23.3508 ^{+1.4} _{-1.0}	23.3503 ^{+1.2} _{-1.1}	23.3505 ^{+1.3} _{-1.1}	23.348 ^{+4.2} _{-4.2}	23.310	...
O III	1s–2p	23.0392 ^{+8.5} _{-5.4}	23.0562 ^{+7.1} _{-8.3}	23.0477 ^{+7.8} _{-7.0}	...	23.0692 ^a	...
Ne I	1s–3p	14.2946 ^{+1.1} _{-3.0}	14.2948 ^{+0.9} _{-0.9}	14.2947 ^{+1.0} _{-2.2}	14.294 ^{+1.5} _{-1.3}	...	14.298
Ne II	1s–2p	14.6077 ^{+0.7} _{-0.7}	14.6077 ^{+0.7} _{-0.7}	14.6077 ^{+0.7} _{-0.7}	14.605 ^{+1.0} _{-1.0}	14.631	14.605
Ne II	1s–3p	14.0038 ^{+1.2} _{-0.9}	14.0037 ^{+1.1} _{-1.1}	14.0037 ^{+1.2} _{-1.0}	14.001 ^{+2.0} _{-1.2}	14.0069 ^a	...
Ne II	1s–4p	13.9382 ^{+1.6} _{-3.1}	13.9345 ^{+3.3} _{-3.0}	13.9363 ^{+2.6} _{-3.1}	...	13.9393 ^a	...
Ne III	1s–2p	14.5077 ^{+0.9} _{-0.8}	14.5079 ^{+0.9} _{-0.9}	14.5078 ^{+0.9} _{-0.9}	14.507 ^{+2.0} _{-2.1}	14.526	14.518
Ne III	1s–3p	13.6960 ^{+1.5} _{-2.4}	13.6959 ^{+1.8} _{-2.5}	13.6959 ^{+1.7} _{-2.5}	13.690 ^{+6.3} _{-1.5}	13.6977 ^a	...
Mg III	1s–3p	9.4339 ^{+44.8} _{-22.1}	9.4772 ^{+1.0} _{-4.2}	9.4555 ^{+31.7} _{-15.9}	...	9.4504 ^a	...

Note. — $\lambda_{i, c}$ ($i = 1, 2$) are the corrected value of the low-ionized elements in Table 4. λ_m is the average value of $\lambda_{i, c}$. The O lines are corrected by $\Delta\lambda_i$ of O I $K\alpha$ in Table 7, and the Ne and Mg lines are both corrected by that of Ne II $K\alpha$. $\sigma_{\lambda_{i, c}}$ are asymmetric; the upper and lower 1σ errors are calculated by $\sigma_{\lambda_{i, c}, j}^2 = \sigma_{\lambda_{i, j}}^2 + \sigma_{\Delta\lambda_i}^2 + \sigma_{\text{sys}}^2$ ($j = u, l$). Values of oxygen in columns 7 and 8 are from García et al. (2005) and Gorczyca (2000) respectively. Values of neon in columns 7 and 8 are from Behar & Netzer (2002) and Gorczyca & McLaughlin (2005) respectively. All the errors are in units of mÅ at 1σ level and ‘*f*’ in parentheses means ‘fixed’.

^a The value obtained from M. Gu (2010, private communication; hereafter Gu10)

Table 9. Comparison of the wavelengths of moderate-ionized elements between the corrected values in this paper, observations in Y09, and the theoretical calculations.

Ion	Transition	$\lambda_{1, c}(\text{\AA})$	$\lambda_{2, c}(\text{\AA})$	$\lambda_m(\text{\AA})$	Y09(\AA)	Gu10(\AA)
O IV	1s–2p	$22.6975^{+3.1}_{-37.3}$	$22.6964^{+3.4}_{-3.4}$	$22.6969^{+3.3}_{-26.5}$...	22.7515
O V	1s–2p	$22.2855^{+4.8}_{-3.4}$	$22.2868^{+3.0}_{-4.2}$	$22.2861^{+4.0}_{-3.8}$...	22.3682
O VI	1s–2p	$22.0287^{+2.6}_{-1.7}$	$22.0289^{+1.9}_{-2.2}$	$22.0288^{+2.3}_{-2.0}$	$22.026^{+4.0}_{-4.0}$	22.0403
Ne IV	1s–2p	$14.3482^{+64.3}_{-64.3}$...	$14.3482^{+64.3}_{-64.3}$...	14.3710
Ne V	1s–2p	$14.2138^{+10.2}_{-38.6}$	$14.2096^{+12.6}_{-13.7}$	$14.2117^{+11.5}_{-29.0}$...	14.2126
Ne VII	1s–2p	$13.8284^{+4.2}_{-2.0}$	$13.8275^{+3.3}_{-4.3}$	$13.8279^{+3.8}_{-3.4}$...	13.8262
Mg IV	1s–2p	$9.8550^{+29.1}_{-1.3}$...	$9.8550^{+29.1}_{-1.3}$...	9.8786
Mg V	1s–2p	$9.8202^{+30.1}_{-30.1}$	$9.8210^{+1.6}_{-2.1}$	$9.8206^{+21.3}_{-21.3}$...	9.8034
Mg V	1s–3p	$9.0581^{+28.0}_{-2.1}$	$9.0559^{+2.6}_{-2.1}$	$9.0570^{+19.9}_{-2.1}$...	9.0766
Fe XVII	2p–3d	$15.0135^{+2.0}_{-1.8}$	$15.0130^{+1.0}_{-1.1}$	$15.0133^{+1.6}_{-1.5}$	15.010(<i>f</i>)	15.015 ^a
Fe XVII	2p–3d	$15.2607^{+1.2}_{-4.3}$	$15.2620^{+2.0}_{-4.6}$	$15.2614^{+1.6}_{-4.5}$...	15.262 ^a

Note. — The same as Table 8, but $\lambda_{i, c}$ ($i = 1, 2$) is the corrected wavelength of the moderate-ionized elements in Table 4. The O lines are corrected by $\Delta\lambda_i$ of O VIII $K\alpha$ in Table 7, and the Ne, Mg, and Fe lines are both corrected by that of Ne IX $K\alpha$. The theoretical calculations of O, Ne, and Mg are obtained from Gu10.

^a The value obtained from NIST.

Table 10. Comparison of the wavelengths of high-ionized elements between the corrected values in this paper, observations in Y09, and the theoretical calculations.

Ion	Transition	$\lambda_{1, c}(\text{\AA})$	$\lambda_{2, c}(\text{\AA})$	$\lambda_m(\text{\AA})$	Y09(\AA)	NIST(\AA)	V96(\AA)
O VII	1s–2p	21.5921 ^{+1.8} _{-1.5}	21.5957 ^{+1.7} _{-1.8}	21.5939 ^{+1.8} _{-1.7}	21.602(<i>f</i>)	21.6020	21.6019
O VII	1s–3p	18.6265 ^{+1.4} _{-1.1}	18.6263 ^{+1.4} _{-1.3}	18.6264 ^{+1.4} _{-1.2}	18.625 ^{+2.6} _{-2.5}	18.6270	18.6288
O VII	1s–4p	17.7663 ^{+1.3} _{-1.5}	17.7682 ^{+1.2} _{-1.5}	17.7673 ^{+1.3} _{-1.5}	17.765(<i>f</i>)	...	17.7686
O VIII	1s–2p	18.9673 ^{+1.0} _{-1.3}	18.9673 ^{+1.1} _{-1.1}	18.9673 ^{+1.1} _{-1.2}	18.964 ^{+2.0} _{-1.7}	18.9689*	18.9689*
O VIII	1s–3p	16.0052 ^{+1.1} _{-1.6}	16.0053 ^{+1.6} _{-1.5}	16.0052 ^{+1.4} _{-1.6}	16.003 ^{+6.7} _{-6.7}	16.0059*	16.0059*
Ne IX	1s–2p	13.4466 ^{+0.7} _{-0.7}	13.4466 ^{+0.7} _{-0.7}	13.4466 ^{+0.7} _{-0.7}	13.445 ^{+1.1} _{-1.2}	13.4470	13.4471
Ne IX	1s–3p	11.5470 ^{+1.5} _{-0.9}	11.5469 ^{+1.7} _{-1.1}	11.5469 ^{+1.6} _{-1.0}	11.549 ^{+1.4} _{-3.4}	11.5470	11.5466
Ne IX	1s–4p	11.0021 ^{+2.6} _{-2.6}	11.0000 ^{+2.0} _{-1.9}	11.0010 ^{+2.3} _{-2.3}	...	11.0128 ^a	...
Ne X	1s–2p	12.1261 ^{+2.2} _{-4.1}	12.1266 ^{+3.0} _{-2.5}	12.1264 ^{+2.6} _{-3.4}	12.134(<i>f</i>)	...	12.1339*
Mg XI	1s–2p	9.1690 ^{+1.0} _{-1.0}	9.1685 ^{+1.0} _{-1.1}	9.1687 ^{+1.0} _{-1.1}	9.170 ^{+0.6} _{-1.2}	9.1689	9.1688

Note. — The same as Table 8, but $\lambda_{i, c}$ ($i = 1, 2$) is the corrected wavelength of the high-ionized elements in Table 4. The O lines are corrected by $\Delta\lambda_i$ of O VIII $K\alpha$ in Table 7, and the Ne and Mg lines are both corrected by that of Ne IX $K\alpha$.

^a The value obtained from Gu10.

* The values of the wavelengths of these lines are the weighted centroids of the doublets in the databases listed in this table.